Local filtration based scatter correction for cone-beam CT using primary modulation

Lei Zhu[a)]
Nuclear and Radiological Engineering and Medical Physics Programs, The George W. Woodruff School of Mechanical Engineering, Georgia Institute of Technology, Atlanta, Georgia 30332 and Department of Modern Physics, School of Physical Sciences, University of Science and Technology of China, Hefei, Anhui 230026, China

(Received 18 April 2016; revised 28 August 2016; accepted for publication 5 October 2016; published 1 November 2016)

Purpose: Excessive scatter contamination fundamentally limits the image quality of cone-beam CT (CBCT), hindering its quantitative use in clinical applications. The author has previously proposed an effective scatter correction method for CBCT using primary modulation. A Fourier transform-based algorithm (FTPM) was implemented to estimate scatter from modulated projections, with a few limitations including the assumption of uniform modulation frequency and magnitude that becomes less accurate in the presence of beam-hardening and other nonideal effects. This paper aims to overcome the above drawbacks by developing a new algorithm for the primary modulation method with improved accuracy and reliability.

Methods: Incident x-ray intensities for each detector pixel with and without the interception of the modulator blocker are estimated from a modulated flat-field image. A new signal relationship is then developed to obtain a first scatter estimate from a modulated projection using a spatially varying modulation distribution. The method empirically adjusts the effective modulation magnitude for each projection ray to account for the beam-hardening effects. Estimated scatter signals with high expected errors are discarded in the generation of the final scatter distribution. The author proposes a technique of local filtration to accelerate major portions of the signal processing, and the new algorithm is referred to as local filtration based primary modulation (LFPM).

Results: The study on the Catphan® 600 phantom shows that LFPM effectively removes scatter-induced cupping artifacts on CBCT images and reduces the CT image error from 222 to 15 HU. In addition, the image contrast on eight contrast rods of the phantom is enhanced by a factor of 2 on average. On an anthropomorphic head phantom, LFPM reduces the CT image error from 153 to 18 HU and eliminates the streak artifacts observed on the result of FTPM with substantially improved image uniformity. On the Rando® phantom, LFPM reduces the CT image error from 278 to 4 HU around the object center.

Conclusions: As compared with the previously developed FTPM algorithm, LFPM enhances the imaging performance by using a more flexible data processing framework that does not require projection data downsampling or uniform modulation frequency and magnitude. It also becomes possible to discard suspicious scatter estimate values prior to the generation of a final scatter distribution and to model the beam-hardening effects on modulation for improved scatter estimation accuracy. The presented research further exploits the potential of the primary modulation method on scatter correction and facilitates its clinical adoption in CBCT imaging. [http://dx.doi.org/10.1118/1.4965042]

Key words: cone-beam CT, scatter correction, primary modulation

1. INTRODUCTION

Scattered photons are a fundamental source of imaging errors on cone-beam CT (CBCT) systems with large-area flat panel detectors. Due to the increasing size of the volume of x-ray irradiation,[1] the average scatter-to-primary ratio (SPR) on a mid-size human torso increases from <0.01 on a 16-slice diagnostic CT scanner to >3 on CBCT systems,[2] which leads to a CT number error of up to ~350 HU.[3–5] Without scatter correction, CBCT images typically contain global cupping artifacts as well as local streaks around dense objects, which greatly hinders the quantitative use of CBCT imaging. This paper aims to design a new data processing algorithm for the primary modulation method,[6–10] a scatter correction technique previously invented by the author, with substantially improved accuracy, flexibility, and reliability.

Scatter correction must be implemented to gain the full benefits of CBCT imaging. The air gap[11] and anti-scatter grid methods[12] prevent scattered photons from reaching the detector but have limited efficacy. Postprocessing methods, by comparison, provide improved scatter suppression; existing methods include analytical calculation,[13,14] Monte Carlo (MC) simulation,[15–18] scatter measurement,[3,19,20] prior-image-based correction,[21,22] and image-domain correction.[23,24] Although these

approaches successfully remove scatter in certain scenarios, the improvement of image quality is often accompanied by method drawbacks including low accuracy, high computational complexity, scan time or patient dose increase, requirement of prior CT images, and reduced image contrasts. A detailed review of scatter correction methods can be found in Ref. 25.

One of the author's previously developed scatter correction techniques, the primary modulation method[6–10] shows great promise for effective scatter removal as a general method on different CBCT systems with no modifications on x-ray tube, detector, or sub-system controls. The method inserts a modulator sheet between the x-ray source and the object to modulate primary signals without shifting the spatial frequency spectrum of scatter. With no increase in data measurement or imaging dose, one effectively estimates and removes scatter based on frequency analysis. Different research groups have demonstrated the success of this method.[26–28] The current signal processing algorithm of primary modulation was developed using the Fourier transform theory, which enables fast computation via filtering techniques. The derivation of the Fourier transform-based primary modulation method (FTPM), however, is established on an assumption of primary signal modulation with uniform modulation frequency and magnitude, which becomes inaccurate in the presence of physical nonidealities, including focal spot wobble, spatially varying x-ray incident angle, and nonuniform beam-hardening effects on the imaged object.

In this paper, the author develops a new algorithm to fully explore the potential of the primary modulation method on scatter correction with no requirements of uniform modulation frequency and magnitude. The algorithm not only allows a more flexible geometry of the primary modulator but also substantially improves the accuracy of scatter correction by using the whole-field projection data and by spatially adjusting the effective modulation magnitude based on the estimated beam-hardening effects. A technique of local filtration is designed to accelerate the computation, and the new method is referred to as local filtration based primary modulation (LFPM). The performance of LFPM is evaluated via phantom studies on a table-top CBCT system.

2. METHOD

2.A. Fourier transform based primary modulation method and its limitations

This section first briefly reviews the scatter correction method using primary modulation and the previous Fourier transform-based algorithm of signal processing, i.e., the FTPM method. More details of method derivation and implementations can be found in the author's early publications.[6–10] The limitations of the FTPM method are then discussed, which leads to the motivation of the presented research on a new signal processing algorithm of scatter correction for CBCT via primary modulation.

2.A.1. The Fourier transform relationship on the modulated projection and the FTPM method

Figure 1(a) shows the imaging geometry of primary modulation. For clarity, only 1D illustrations are drawn. A primary modulator with a high-frequency pattern, which consists of an array of x-ray semitransparent blockers, is inserted between the object and the x-ray source. Primary signals are modulated by the same frequency pattern. We have shown that a modulator period of up to 27 mm on the detector is adequate for accurate scatter estimation in a clinical CBCT geometry.[9] In the FTPM algorithm, we use only the data at the centers of high- and low-intensity regions on the detector to avoid the edge effect of the modulator. The downsampled primary signals, which have alternating transmission ratios in neighboring pixels, have the following relationship:

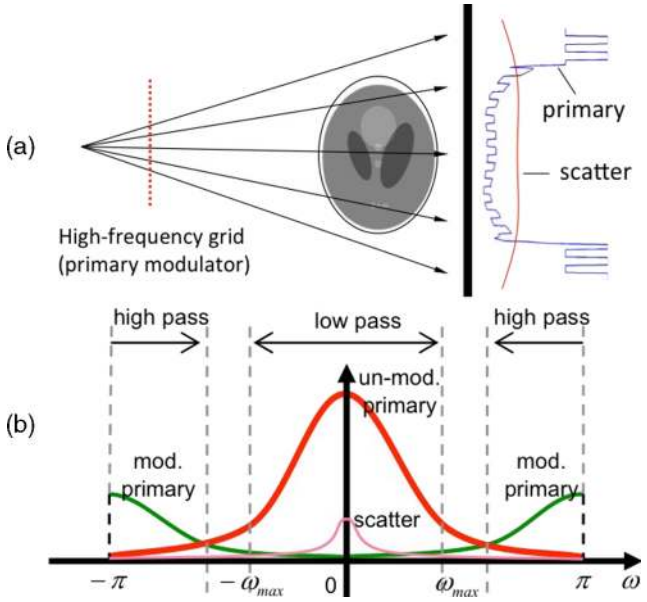

FIG. 1. Illustrations of the primary modulation method for scatter correction and the Fourier transform-based algorithm of signal processing. (a) System geometry with the insertion of primary modulator. Primary signals are modulated while scatter signals are still dominated by low-frequency components. (b) Signals in the Fourier domain, showing that scatter and the modulated primary are mostly nonoverlapping (courtesy of Dr. Hewei Gao).

$$p'(i,j) = p(i,j)\cdot\frac{1+\alpha}{2} + p(i,j)\cdot\frac{(1-\alpha)\cdot(-1)^{i+j}}{2}, \tag{1}$$

where p and p' are the primary signals before and after modulation, respectively, (i,j) is the pixel index in the image domain, and α is the transmission ratio at the center of the modulator blockers (ranging from 50% to 90% for different primary modulators in our published experiments). Taking the discrete Fourier transform (DFT) on both the sides of Eq. (1), we get

$$P'(u,v) = P(u,v)\cdot\frac{1+\alpha}{2} + P(u-\pi,v-\pi)\cdot\frac{(1-\alpha)}{2}, \tag{2}$$

where upper-case P and P' are the DFT of the primary signals and (u,v) is the index in the Fourier domain. Equation (2) shows that primary signals are partially modulated to the high-frequency region, with a ratio of $(1-\alpha)/(1+\alpha)$ to the unmodulated primary. Barring statistical noise, studies have shown that scatter is still dominantly low-frequency even if high-frequency components are present in the x-ray source distribution.[9] If the sampling of the projection field is uniform (i.e., the distance

between the centers of high- and low-intensity regions on the detector is constant), the downsampled scatter signals contain dominant low-frequency components as well. The modulated primary signals therefore bypass scatter contamination. Figure 1(b) shows the primary and scatter distributions after primary modulation.

For scatter correction via FTPM, we first extract the modulated primary via high-pass filtering, demodulate to low frequency, and then divide by the premeasured modulation fraction, i.e., $(1-\alpha)/(1+\alpha)$, to get the low-frequency primary signals. We then apply low-pass filtering on raw projections and subtract the estimated low-frequency primary. The resultant scatter estimate is upsampled to full resolution. Standard filtered-backprojection (FBP) reconstruction is performed on scatter-corrected projection data. A ring correction algorithm is used to remove possible ring artifacts induced by the modulator.[29,30] Details of algorithm implementation can be found in Refs. 6–10.

2.A.2. Limitations of the FTPM method

Since the FTPM method as reviewed above uses DFT in signal processing, the extra computational cost required for scatter correction is negligible compared with that of CBCT reconstruction. Despite its theoretical elegance and success as demonstrated in a few publications by different research groups,[6–10,26,27,31] however, several limitations should be noted on FTPM. First, FTPM requires projections to be downsampled for signal processing. The significantly reduced size of measurement data lowers the capability of the primary modulation method on estimating relatively high-frequency scatter signals. Second, the FTPM method design is based on the sampling theory and the relationship shown in Eq. (1). The accuracy of FTPM therefore heavily relies on the following implicit assumptions on the primary modulator across the projection field: (1) the distance between the centers of high- and low-intensity regions on the detector is constant, and (2) the blocker transmission ratio α is constant. In practical implementations, however, it is challenging to manufacture a primary modulator that satisfies these two conditions, mainly due to the nonuniform spatial distributions of the x-ray source intensity and the detector response, as well as the spatially varying incident angles in a divergent beam of CBCT. Furthermore, note that, on a commercial CBCT system with a polychromatic x-ray source, different thicknesses of the imaged object on different projection rays lead to different levels of beam-hardening effects. Therefore, the effective transmission ratio of a primary modulator spatially varies on the projections of an object, even if the modulator is well designed with a constant sampling period and a uniform transmission ratio in a flat-field image. Finally, FTPM processes the signal of each pixel in an equal manner and it lacks a capability of removing scatter estimates in certain areas of high expected errors. After filtering procedures of FTPM, local scatter estimation errors become global. One particular example is the high scatter estimation errors around the object boundary where primary signals contain high-frequency components, and therefore scatter estimation via primary modulation becomes inaccurate. In the previous publication,[9] an auxiliary boundary detection algorithm was used to empirically suppress the high potential errors of scatter estimation around the object boundary on the detector.

2.B. Local filtration based primary modulation method for scatter correction

The author aims to develop a new signal processing algorithm of primary modulation, i.e., the LFPM method, with improved scatter correction accuracy and stability. LFPM has the following new features compared with FTPM:

(1) All projection data are used for scatter correction, with no requirement of downsampling.
(2) An arbitrary modulation pattern of the primary modulator is allowed, with no constraint of uniform modulation frequency and magnitude.
(3) Effective beam hardening correction can be integrated for more accurate scatter estimation.
(4) Local scatter estimates with high expected errors can be discarded during the signal processing to improve the global scatter estimation accuracy.

2.B.1. A new signal relationship on the modulated projection and the local filtration technique

LFPM still adopts an imaging geometry with a primary modulator inserted between the x-ray source and the imaged object. Different from the FTPM method, the x-ray semitransparent blockers of the modulator are not required to be evenly spaced or with the same effective attenuation. We denote $I_{0h}(i,j)$ and $I_{0l}(i,j)$ as the incident x-ray intensity for one projection ray at (i,j) without and with the interception of the modulator blocker, respectively. On the detector, the corresponding measured projections on one object are $p_h(i,j)$ and $p_l(i,j)$, with the scatter signals $s_h(i,j)$ and $s_l(i,j)$, respectively. If the beam-hardening effects on an imaged object are ignored (this condition will be relaxed later), the following equation holds due to the unchanged blocker transmission ratio $\alpha(i,j)$ with and without the imaged object:

$$\alpha(i,j)=\frac{I_{0l}(i,j)}{I_{0h}(i,j)}=\frac{p_l(i,j)-s_l(i,j)}{p_h(i,j)-s_h(i,j)}. \tag{3}$$

On one projection image with the insertion of the primary modulator, we have one single distribution of scatter signals, i.e., $s(i,j)=s_l(i,j)=s_h(i,j)$. However, Eq. (3) cannot be directly used for scatter estimation, because each projection ray lacks the measurement of either p_h or p_l. Since p_h and p_l are interlaced on the modulated projection, we can estimate the missing p_h or p_l from the neighboring data, as illustrated in Fig. 2. The full-size I_{0h} or I_{0l} can be estimated on I_0, the flat-field projection with the primary modulator inserted, in a similar way. Denoting the estimated data as $\widehat{(\cdot)}$, we derive the scatter estimation formula from Eq. (3) as

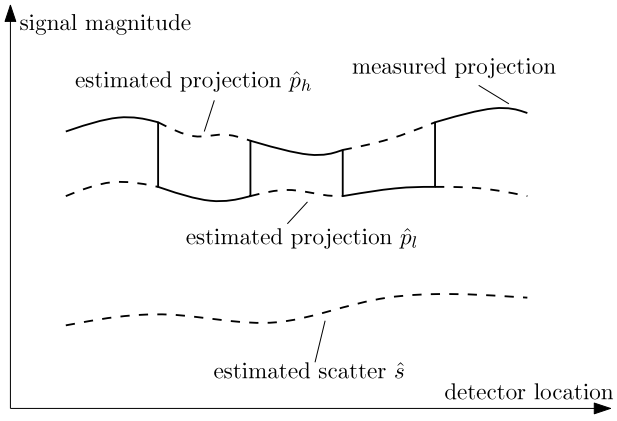

FIG. 2. 1D illustration of measured and estimated signals used in the derivation of LFPM.

$$\frac{\widehat{I_{0l}}(i,j)}{\widehat{I_{0h}}(i,j)} = \frac{\widehat{p_l}(i,j)-\hat{s}(i,j)}{\widehat{p_h}(i,j)-\hat{s}(i,j)} \Rightarrow$$
$$\hat{s}(i,j) = \left(\widehat{p_l}(i,j) - \frac{\widehat{I_{0l}}(i,j)}{\widehat{I_{0h}}(i,j)}\widehat{p_h}(i,j)\right) \Big/ \left(1 - \frac{\widehat{I_{0l}}(i,j)}{\widehat{I_{0h}}(i,j)}\right). \quad (4)$$

To obtain $\widehat{I_{0l}}$, $\widehat{I_{0h}}$, $\widehat{p_l}$, and $\widehat{p_h}$ in Eq. (4), we first determine from the flat-field image I_0 the high-intensity and low-intensity detection areas, Ω_h and Ω_l, on the modulated projection field. The base-line image of I_0 is calculated via Gaussian smoothing as

$$\overline{I_0}(i,j) = \frac{\sum_s \sum_t I_0(s,t) w_\sigma(i-s,j-t)}{\sum_s \sum_t w_\sigma(i-s,j-t)} = I_0 ** w_\sigma', \quad (5)$$

where ** denotes the 2D convolution operation, w_σ' is the normalized function of w_σ, and w_σ is defined as

$$w_\sigma(s,t) = e^{-\frac{(s^2+t^2)}{\sigma^2}}, \quad (6)$$

where σ in Eq. (6) is a user defined parameter that specifies the width of the Gaussian kernel. All the algorithm parameters used in the implementations presented in this paper will be summarized in a later section. Ω_h and Ω_l are then determined by thresholding the deviation of the flat-field intensity from the base-line value

$$\Omega_h = \left\{(i,j) | I_0(i,j) > (1+T)\cdot \overline{I_0}(i,j)\right\},$$
$$\Omega_l = \left\{(i,j) | I_0(i,j) < (1-T)\cdot \overline{I_0}(i,j)\right\}, \quad 0<T<1, \quad (7)$$

where T is another user defined parameter.

$\widehat{I_{0l}}$ (or $\widehat{I_{0h}}$) is obtained via weighted summation of available data in the low-intensity region, Ω_l (or in the high-intensity region, Ω_h), as

$$\widehat{I_{0l/h}}(i,j) = \frac{\sum_{(s,t)\in\Omega_{l/h}} I_0(s,t) w_\gamma(i-s,j-t)}{\sum_{(s,t)\in\Omega_{l/h}} w_\gamma(i-s,j-t)}, \quad (8)$$

where w_γ is a Gaussian function as defined in Eq. (6) with a different width of the Gaussian kernel, γ. The calculation of Eq. (8) is equivalent to signal smoothing in Ω_l (or Ω_h) and interpolation outside. Similarly, from the measured projection p_m with the insertion of primary modulator, $\widehat{p_l}$ and $\widehat{p_h}$ are estimated as

$$\widehat{p_{l/h}}(i,j) = \frac{\sum_{(s,t)\in\Omega_{l/h}} p_m(s,t) w_\gamma(i-s,j-t)}{\sum_{(s,t)\in\Omega_{l/h}} w_\gamma(i-s,j-t)}. \quad (9)$$

To facilitate the computation of Eqs. (8) and (9), indicator functions, f_l and f_h, are defined as

$$f_{l/h}(i,j) = \begin{cases} 1, & \text{if } (i,j)\in\Omega_{l/h}, \\ 0, & \text{otherwise.} \end{cases} \quad (10)$$

It is easily verified that Eqs. (8) and (9) can be calculated via convolution

$$\widehat{I_{0l/h}}(i,j) = \frac{(I_0\cdot f_{l/h}) ** w_\gamma}{f_{l/h} ** w_\gamma}, \quad (11)$$

$$\widehat{p_{l/h}}(i,j) = \frac{(p_m\cdot f_{l/h}) ** w_\gamma}{f_{l/h} ** w_\gamma}. \quad (12)$$

Scatter estimation via Eq. (4) therefore consists of signal filtration operations as shown in Eqs. (11) and (12).

Equations (11) and (12) [or Eqs. (8) and (9)] are developed to estimate the complete distributions of the flat-field or the projection signals at two different x-ray spectra from one single projection with the insertion of a primary modulator. The modulation pattern divides the projection field into the measured and the unknown areas for one particular target distribution. Inside the measured area, Eq. (11) or Eq. (12) is simply a smoothing process via filtration only on the local measured data by a Gaussian kernel; inside the unknown area, although still in the form of signal filtration, it becomes signal estimation via interpolation from the neighboring measured signals. This step of signal processing is therefore referred to as local filtration, and the proposed algorithm

TABLE I. LFPM algorithm parameters and their values used in the phantom studies presented in this paper.

Parameter	Description	Catphan® 600	Head	Rando®
σ	Gaussian kernel width used to generate $\overline{I_0}$ in Eq. (5)	40 pixels		
T	Threshold to determine Ω_h and Ω_l in Eq. (7)	0.14		
γ	Gaussian kernel width used to generate $\widehat{I_{0l}}$ and $\widehat{I_{0h}}$ in Eq. (11), $\widehat{p_l}$ and $\widehat{p_h}$ in Eq. (12)	3 pixels		
η	Coefficient for beam-hardening compensation in Eq. (13)	0.01	0.02	0.01
U	Threshold to determine Γ in Eq. (14)	50 counts	50 counts	120 counts
β	Gaussian kernel width used to generate $\widehat{sf}$ in Eq. (16)	13 pixels	9 pixels	9 pixels

for scatter correction using primary modulation is referred to as LFPM. It is worth emphasizing that, since the equations of local filtration are in the form of image convolution, they can be efficiently computed via fast Fourier transform techniques.

2.B.2. Scatter estimation errors and empirical error-suppression methods

An estimate of the scatter signals can be obtained using Eq. (4), which is based on Eq. (3), assuming that the effective transmission ratio of the modulator blocker is unaffected by different levels of beam-hardening effects on the object. In reality, the beam-hardening effect increases the mean x-ray energy, and thus lowers the attenuation of the modulator blocker compared to that measured on a flat-field image. As a result, the projection signals measured or estimated behind the modulator blocker, i.e., $\widehat{p_l}(i,j)$ in Eq. (4), become higher than the theoretical values, leading to scatter over-estimation.

The author proposes to improve the scatter estimation accuracy using empirical compensation for the beam-hardening effect. As the measured attenuation of each projection ray, p_m/I_0, indicates the level of beam-hardening effect, Eq. (4) is modified as

$$\hat{s}(i,j)=\left(\left(\frac{p_m(i,j)}{I_0(i,j)}\right)^{\eta}\widehat{p_l}(i,j)-\frac{\widehat{I_{0l}}(i,j)}{\widehat{I_{0h}}(i,j)}\widehat{p_h}(i,j)\right)/\left(1-\frac{\widehat{I_{0l}}(i,j)}{\widehat{I_{0h}}(i,j)}\right), \tag{13}$$

where η is an empirical parameter controlling the strength of data correction.

Scatter estimation via Eq. (13) still contains large errors mainly because roughly half data of $\widehat{I_{0l/h}}$ and $\widehat{p_{l/h}}$ are estimated via interpolation. On the other hand, barring statistical noise, scatter in a cone-beam projection contains dominant low spatial-frequency components,[13,15] implying that an accurate whole-field scatter distribution can be estimated from a small number of scatter samples. As such, one can discard the scatter data obtained from Eq. (13) that have high expected estimation errors and generate a new estimate of scatter distribution from the data only in the "trusted" areas. Note that, a good estimate of scatter should be positive and smaller than the measured projection (otherwise, the estimated primary signal becomes negative). In addition, as interpolation is used in Eq. (12), large errors are expected on $\widehat{p_{l/h}}$ (therefore on $\hat{s}$) in the area where $\widehat{p_{l/h}}$ has large gradients. The area of accurate scatter estimation is therefore defined as

$$\Gamma=\{(i,j)|(i,j)\in\Omega_l\cup\Omega_h,\quad 0<\hat{s}(i,j)<p_m(i,j),\quad |\nabla\widehat{p_l}(i,j)|<U,\quad \text{and}\quad |\nabla\widehat{p_h}(i,j)|<U\}, \tag{14}$$

where Ω_h and Ω_l are the high-intensity and low-intensity detection areas obtained from the flat-field image, $|\nabla(\cdot)|$ calculates the magnitude (i.e., length) of the gradient vector on a 2D image, and U is a threshold parameter on the gradient magnitude.

The local filtration technique as described in Sec. 2.B.1 is then used to obtain a whole-field scatter distribution from only the estimated scatter signals in Γ. A new indicator function, g, is defined as

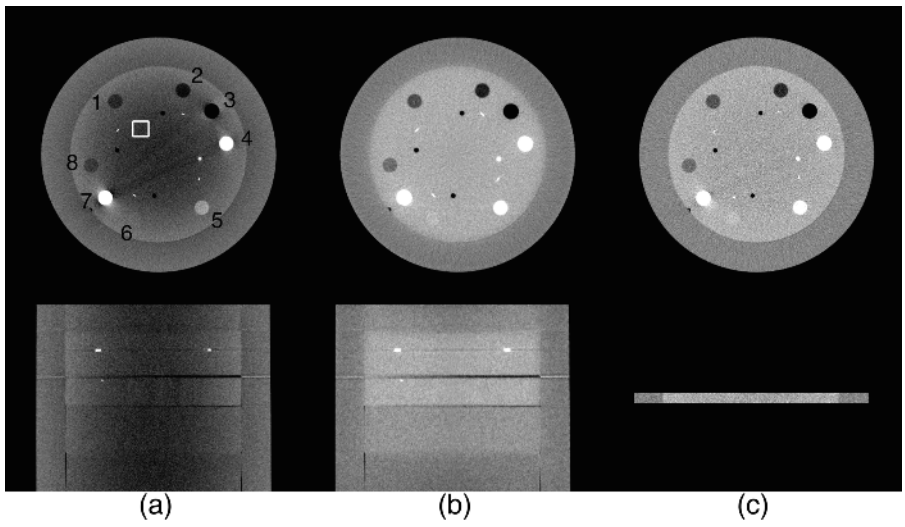

FIG. 3. Comparison of CT images of the Catphan® 600 phantom. (a) CBCT without scatter correction; (b) CBCT with scatter correction using LFPM; (c) FBCT. Top row: axial images; bottom row: coronal images. Display window: [-250 250] HU. The labels in the axial image of (a) indicate the contrast rods used in the image contrast measurements shown in Table II. The mean CT image values measured inside the white square are (a) −151 HU, (b) 86 HU, and (c) 71 HU; the standard deviations are (a) 28 HU, (b) 21 HU, and (c) 42 HU.

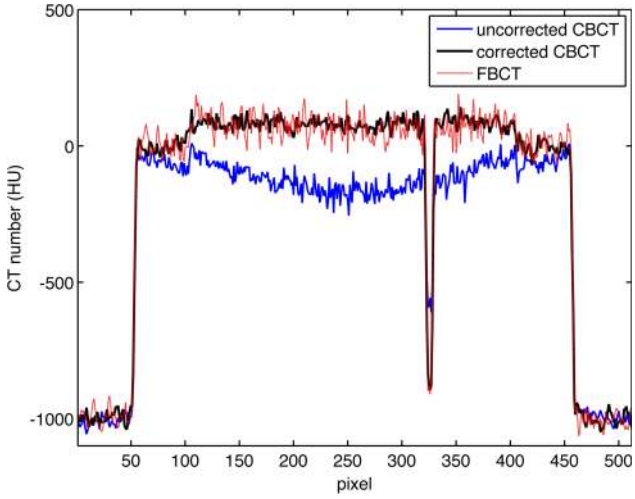

FIG. 4. Comparison of central vertical 1D profiles taken on the axial CT images shown in Fig. 3.

$$g(i,j)=\begin{cases}1, & \text{if } (i,j)\in\Gamma,\\ 0, & \text{otherwise.}\end{cases} \tag{15}$$

The final scatter estimate is obtained as

$$\widehat{s_f}(i,j)=\frac{(\hat{s}\cdot g)**w_\beta}{g**w_\beta}, \tag{16}$$

where w_β is a Gaussian function as defined in Eq. (6) with a kernel width, β.

2.B.3. Summary of the LFPM method

The workflow of the LFPM method is summarized as follows:

At the stage of system calibration:

(1) Measure a flat-field image I_0 with the insertion of a primary modulator and obtain the baseline image $\overline{I_0}$ using Gaussian filtration, Eq. (5).
(2) Determine the high- and low-intensity detection areas, Ω_h and Ω_l, via thresholding, Eq. (7).
(3) Estimate the high- and low-intensity flat-field images, $\widehat{I_{0l}}$ and $\widehat{I_{0h}}$, using local filtration, Eq. (11).

On each modulated projection p_m:

(4) Estimate the high- and low-intensity projections, $\widehat{p_l}$ and $\widehat{p_h}$, using local filtration, Eq. (12).
(5) Generate a first estimate of scatter, $\hat{s}$, using Eq. (13).
(6) Estimate the area of accurate scatter estimation, Γ, via thresholding, Eq. (14).
(7) Generate the final scatter estimate, $\widehat{s_f}$, using local filtration, Eq. (16).
(8) Apply a softcut function[9] on $\widehat{s_f}$ and subtract it from the modulated projection p_m to obtain a primary estimate.

After scatter correction on all projections:

(9) Reconstruct CBCT images using a conventional reconstruction algorithm (e.g., FDK).
(10) Apply ring correction[29,30] on the reconstructed images to remove possible ring artifacts induced by the modulator.

The softcut function used in Step (8), which has the same design as in the previous publication,[9] ensures that the scatter estimate is smaller than the measured projection and thus the estimated primary always has positive values. Fast Fourier transform is used to accelerate the computation of local filtration [i.e., Eqs. (11), (12), and (16)], the procedure with the highest computational complexity in the proposed algorithm. Therefore, the overall signal processing of LFPM can be carried out very efficiently on a standard PC. Compared with FTPM, another difference in LFPM is that the suppression of high-frequency components on the object boundary via auxiliary boundary detection[9] is unnecessary, since LFPM can selectively remove intermediate scatter estimates in the area of high expected errors in Step (6).

2.C. Evaluation

We evaluate the method performance on three physical phantoms, the Catphan® 600 phantom (The Phantom Laboratory, Salem, NY), an anthropomorphic head phantom and the Rando® phantom (Imaging Solutions, Cypress, TX). Projection data are acquired on our table-top CBCT system at Georgia Institute of Technology, of which the geometry exactly matches that of the on-board imager of a Varian clinical linear accelerator. The flat-panel detector has an effective size of 40 $\times$ 30 cm^2 with 1024 $\times$ 768 pixels. No anti-scatter grid is installed on the detector. The x-ray source has a distance of 100 cm to the rotational center and a distance of 150 cm to the detector. Each CT scan contains 655 equi-angular projections on a 360-degree rotation. The x-ray tube is operated at 125 kVp, with a tube current of 80 mA and a pulse width of 7 ms. More description about the system can be found in Ref. 20.

In all studies, we compare the results of CBCT imaging with and without the primary modulation-based scatter correction. The copper modulator as designed in Ref. 6 is used in the presented investigations. On a flat-field image, the blockers

TABLE II. Image contrasts (in HU) measured on different contrast rods shown in the axial images of Fig. 3. Inside parentheses are the contrast increase ratios compared with the results of no scatter correction, i.e., the first row.

Rod index	1	2	3	4	5	6	7	8
No correction, Fig. 3(a)	101	152	586	421	121	9	1045	69
LFPM, Fig. 3(b)	183 (1.808)	272 (1.788)	1064 (1.817)	878 (2.088)	248 (2.060)	23 (2.476)	2488 (2.381)	120 (1.741)
FBCT, Fig. 3(c)	178 (1.765)	254 (1.674)	978 (1.670)	782 (1.858)	222 (1.838)	30 (3.247)	2137 (2.045)	120 (1.744)

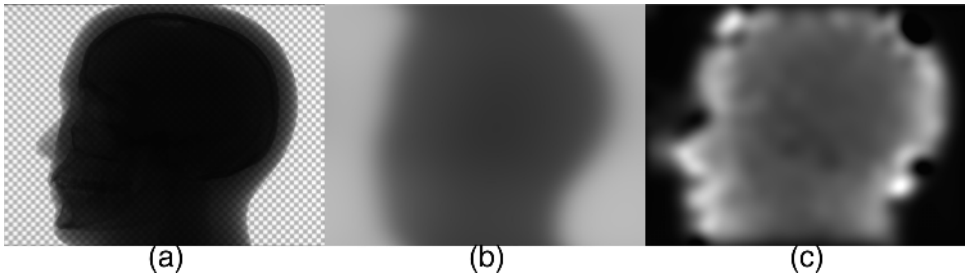

FIG. 5. Projection image and estimated scatter distributions on the anthropomorphic head phantom. (a) Projection image with insertion of the primary modulator; (b) estimated scatter distribution using LFPM; (c) estimated scatter distribution using FTPM. Display window: (a) [min max]; (b) and (c) [0 4000] detector counts.

on the modulator have measured transmission ratios of around 70% and center-to-center spacing of about 30 pixels on the detector. Fan-beam CT (FBCT) images, which are acquired with a narrow collimator in the longitudinal direction (a width of about 15 mm on the detector) to inherently suppress scatter, are considered as scatter-free references. On the anthropomorphic head phantom, the projection data contain more beam-hardening errors due to the presence of bone structures. The complicated phantom geometry increases the spatial variation of scatter distributions. These challenges make FTPM more error-prone. In the study of the anthropomorphic head phantom, we compare the scatter correction results via the primary modulation technique using both FTPM and LFPM algorithms. CT image volumes are reconstructed by the standard FDK algorithm with $512\times512\times320$ pixels and $0.5\times0.5\times0.5$ mm^3 pixel size. Note that, in the FBCT reconstruction, accurate images are available only in the central 18 axial slices due to the narrow collimator.

CT image accuracy and contrast are used as the quality metrics. We measure the CT image error in a selected uniform region of interest (ROI) as

$$E = |\mu_c - \mu_f|, \tag{17}$$

where μ_c and μ_f are the mean values in Hounsfield unit (HU) inside the ROI of the CBCT image and the FBCT image, respectively. In the study of the Catphan® 600 phantom, we measure image contrasts as the signal differences (absolute values) between the mean image values inside and outside eight contrast rods.

Both the LFPM algorithm proposed in this paper and the original FTPM algorithm are implemented in MATLAB. On a Macbook Pro with a processor of 2.6 GHz Intel Core i5, it takes about 400 and 150 ms to complete scatter correction on one raw cone-beam projection for LFPM and FTPM, respectively.

Table I lists all the parameters of the LFPM method, and their values used in the implementations shown in this paper. To facilitate readers' implementations of the proposed algorithm on different CT systems, the parameter values in Table I are given in unit of either detector pixels or detector counts. All the six algorithm parameters are empirically selected. The spacing and the thickness of modulator blockers control the spatial distribution of high- and low-intensity areas on the detector and their signal levels. Parameters σ, T, and γ remain unchanged in this paper but need to be tuned for different designs of primary modulator. Parameters η, U, and β are mainly determined by the beam-hardening effects and the properties of scatter distributions on the imaged object, and thus may need adjustments in different studies.

3. RESULTS

3.A. Catphan® 600 phantom results

Figure 3 shows the axial and the coronal views of the CT reconstructions of the Catphan® 600 phantom without and with scatter correction via LFPM, and with a fan-beam geometry. Figure 4 compares the central vertical 1D profiles taken on the axial CT images shown in Fig. 3. Although acquired at the same x-ray tube setting, the projection data used to reconstruct the above CT images have different noise levels. The primary modulator reduces the total number of photons reaching the scanned object. Furthermore, as a postprocessing method, scatter correction via primary modulation increases the noise level of the CT images due to the remaining scatter noise on the corrected projections.[4] In this study, our previously developed penalized weighted least square (PWLS) algorithm[4] is used for noise suppression on the scatter-corrected CT images, so that Figs. 3(a) and 3(b) have similar noise levels.

As evident in both Figs. 3 and 4, LFPM substantially suppresses the cupping artifacts on the uncorrected CBCT images and obtains an improved image quality matching that of FBCT. In the selected ROI [indicated by the rectangle in Fig. 3(a)], the proposed method reduces the CT image error from 222 HU down to 15 HU. Table II lists the measured contrasts of different CT images for the eight contrast rods labeled in Fig. 3(a). The contrast increase ratios on the scatter-corrected image and FBCT compared with the uncorrected

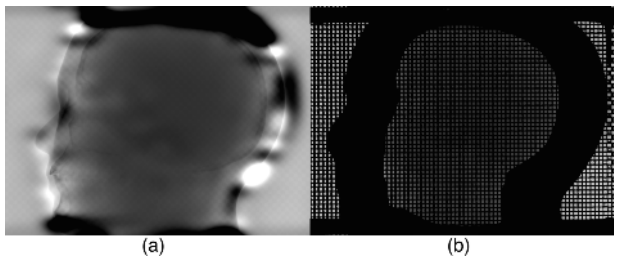

FIG. 6. Estimated scatter distributions in the intermediate steps of the LFPM algorithm. (a) First scatter estimate using Eq. (13); (b) scatter signals used for local filtration. The original signals in the dark area of (b) are discarded using Eq. (14) and do not contribute to the final scatter estimation. Display window: [0 4000] detector counts.

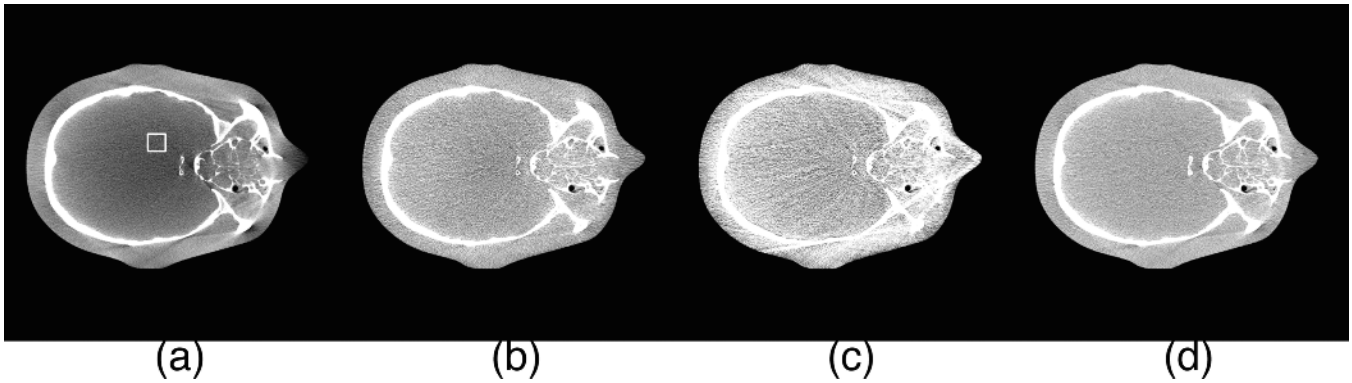

FIG. 7. Axial CT images of the anthropomorphic head phantom. (a) CBCT without scatter correction; (b) CBCT with scatter correction using LFPM; (c) CBCT with scatter correction using FTPM; (d) FBCT. Display window: [−250 250] HU. The mean CT image values measured inside the white square are (a) −81 HU, (b) 54 HU, (c) 91 HU, and (d) 72 HU; the standard deviations are (a) 31 HU, (b) 66 HU, (c) 91 HU, and (d) 46 HU.

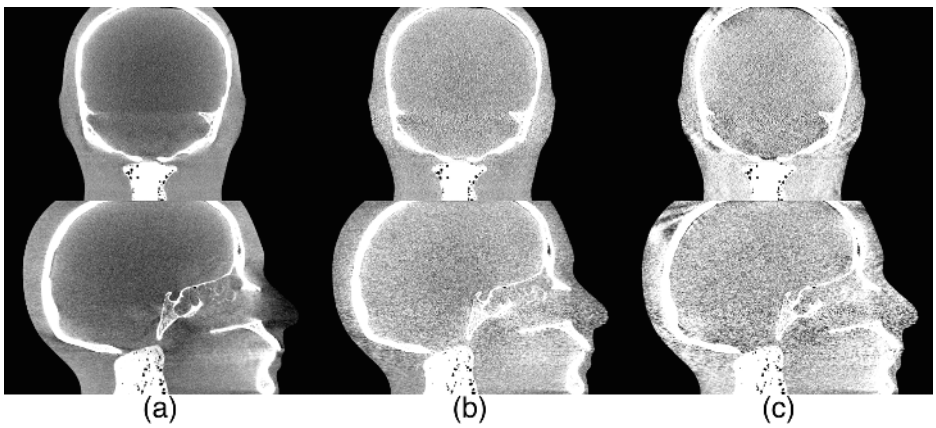

FIG. 8. Coronal (top row) and sagittal (bottom row) CT images of the anthropomorphic head phantom. (a) CBCT without scatter correction; (b) CBCT with scatter correction using LFPM; (c) CBCT with scatter correction using FTPM. Display window: [−250 250] HU.

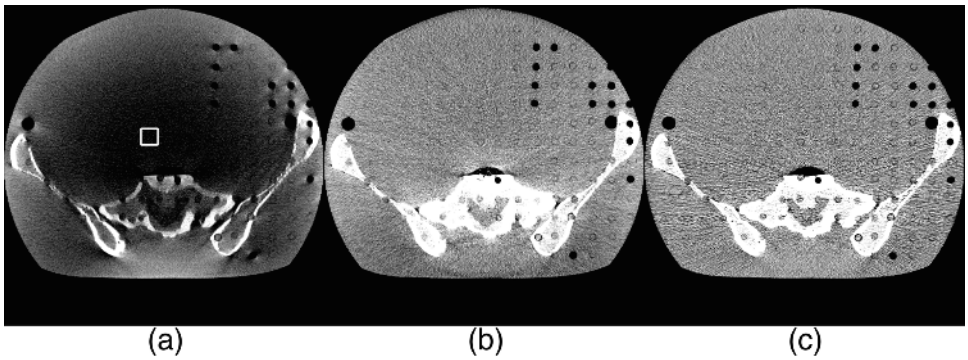

FIG. 9. Axial CT images of the Rando® phantom. (a) CBCT without scatter correction; (b) CBCT with scatter correction using LFPM; (c) FBCT. Display window: [−250 250] HU. The mean CT image values measured inside the white square are (a) −260 HU, (b) 14 HU, and (c) 18 HU; the standard deviations are (a) 43 HU, (b) 70 HU, and (c) 92 HU.

CBCT image are shown in parentheses. On average, LFPM and FBCT increase the image contrasts by a factor of 2.02 and 1.98, respectively, indicating a high efficacy of scatter correction using the proposed method.

3.B. Anthropomorphic head phantom results

As shown in our previous publication,[9] FTPM effectively removes scatter in CBCT projections and obtains a superior CT image quality on objects with simple geometries (e.g., the Catphan® 600 phantom). The performance of FTPM, however, degrades on objects that contain dense materials (e.g., bones) with complex structures. Projections on these objects have large beam-hardening errors and relatively high spatial variations on scatter distributions, both of which substantially reduce the scatter estimation accuracy of FTPM. The above challenge is well observed in the CBCT scan on the anthropomorphic head phantom. Figure 5 shows one measured

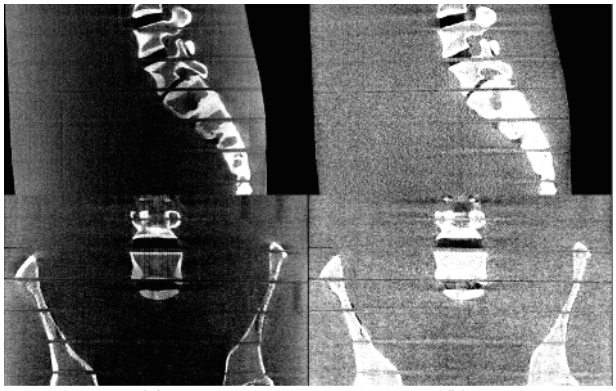

FIG. 10. Sagittal (top row) and coronal (bottom row) CT images of the Rando® phantom. (a) CBCT without scatter correction; (b) CBCT with scatter correction using LFPM. Display window: [−250 250] HU.

raw projection with primary modulation and its corresponding scatter estimates using LFPM and FTPM. Note that, the estimated scatter signals using FTPM are low outside the object boundary due to the signal suppression of the auxiliary boundary detection step.[9] These signals are recovered to a correct high level in the result of LFPM, where no boundary detection is needed. It is seen that, compared with LFPM, FTPM obtains an estimated scatter distribution that appears more irregular. In the result of FTPM, most suspicious areas of high scatter estimation errors are where the measured raw projection has high spatial variations (e.g., object boundary).

The new LFPM algorithm is able to suppress large scatter estimation errors that appear in FTPM. Figure 6 shows that the estimated scatter distributions in the intermediate steps of LFPM. The first scatter estimate obtained from Eq. (13) [Fig. 6(a)] contains large errors around bone areas and object boundaries. The proposed Eq. (14) removes most of these untrusted scatter estimates [see Fig. 6(b)], and the local filtration technique finally obtains a scatter distribution shown in Fig. 5(b).

The efficacies of scatter estimation and removal using LFPM and FTPM are compared on the corrected CBCT images shown in Figs. 7 and 8. To investigate the imaging performance on small bony structures, the PWLS noise suppression on the projection data is disabled in this study. In the selected ROI [indicated by the rectangle in Fig. 7(a)], both LFPM and FTPM effectively remove scatter and reduce the CT image error from 153 to 18 and 19 HU, respectively. However, due to scatter estimation errors in the projection areas where the spatial variation of primary signals is high and the beam-hardening errors are large, the corrected CBCT images obtained by FTPM show strong streak artifacts around bones. It is prominent that LFPM achieves a substantially improved performance with better image uniformity and less image artifacts.

3.C. Rando® phantom results

The Rando® phantom represents a very challenging case of CBCT scatter correction due to the high magnitude of scatter signals in each projection. In our experiment, the measured SPR in a cone-beam projection on the Rando® phantom reaches up to around 9 behind highly attenuating bony structures, with an average of around 3–4 at the detector center. Figures 9 and 10 compare the CBCT images with and without correction and the FBCT image as a reference. The PWLS algorithm[4] is used for noise suppression on the CBCT images with scatter corrected by LFPM. A cylindrical fitting method[32] is employed to reduce reconstruction errors from signal truncation on the detector. With strong shading and cupping artifacts induced by scatter, the uncorrected CBCT image has a CT number error of 278 HU at the object center. LFPM successfully reduces the error down to 4 HU via scatter removal. In the corrected CBCT, some image nonuniformity is observed around bones. The projection rays passing through this area have extremely high SPRs (>7), which make scatter correction and PWLS noise suppression more demanding.

4. CONCLUSIONS AND DISCUSSION

In this paper, the author proposes a new algorithm of signal processing, LFPM, for scatter correction in CBCT imaging using primary modulation. As compared with the previously developed FTPM algorithm, LFPM enhances the imaging performance by using a more flexible data processing framework that does not require projection data downsampling or uniform modulation magnitude and frequency. It also becomes possible to discard suspicious scatter estimates prior to the generation of a final scatter distribution and incorporate an empirical beam-hardening effect estimation to improve the scatter estimation accuracy. The study on the Catphan® 600 phantom shows that LFPM effectively removes scatter-induced cupping artifacts on CBCT images and reduces the CT image error from 222 to 15 HU. In addition, the image contrasts on the eight contrast rods are enhanced by a factor of 2 on average. On the anthropomorphic head phantom, LFPM reduces the CT image error from 153 to 18 HU and eliminates the streak artifacts observed on the result of FTPM with substantially improved image uniformity. On the Rando® phantom, LFPM reduces the CT image error from 278 to 4 HU around the object center.

The main purpose of this paper is to develop a flexible framework of signal processing for scatter correction via primary modulation based on a new signal relationship on modulated CBCT projections and to demonstrate its performance in proof-of-concept studies. The proposed method can be further improved in different aspects. The current LFPM uses a simple and empirical exponential function to estimate the effects of beam hardening on the measured projection data. As shown in the results of the Rando® phantom, this technique needs further improvement when the scanned object contains dense materials and the SPR on projections is high. A more sophisticated model, as used in the beam-hardening correction of CT imaging,[33] will increase the scatter estimation accuracy. Since the signal modulation is not required to be uniform in LFPM, one may use an irregular modulation pattern to optimize scatter correction. For example, dense modulation should be used in the detector area where the object boundary is located, and

strong modulation should be used around the object center where SPR is high. All the above possible improvements are of high interest in our future studies.

It is a known issue that the originally designed FTPM algorithm is very sensitive to the uniformity of the modulation frequency and magnitude.[28,31] One research group has recently proposed an iterative approach to make the primary modulation method more robust.[28] The separation of scatter from primary signals is modeled as an optimization problem with the constraints that the estimated scatter distribution should be smooth and the estimated primary signal should match the premeasured modulation pattern. To improve the computational efficiency and lower the memory consumption, raw projection images are divided into small patches for separate signal processing. The LFPM algorithm proposed in this paper aims to improve the reliability and accuracy of the primary modulation method using a different approach. LFPM consists of a few procedures of standard image filtration and therefore has a high computational efficiency without memory burden. In addition, LFPM allows the removal of wrong scatter estimates during the signal processing and models beam-hardening effects for better scatter estimation accuracy. The improved robustness, as achieved by LFPM presented in this paper and by other research groups, facilitates the translation of the primary modulation method from theory to clinical practice.

It should be noted that, in addition to algorithmic improvements, more investigations are still needed on the primary modulation technique toward its implementations on clinical CT systems. For example, gantry vibration and focal spot wobble result in penumbra effects on the beam blocker edges, which limit the highest modulation frequency for accurate scatter estimation. The design of a primary modulator therefore should be customized for different CT systems for optimal performance. An x-ray tube generates secondary scatter from off-focal radiation on the target,[34,35] as well as photon interactions with housing, inherent filter, and primary modulator. Our future research will include studies on the effect of off-focal radiation on primary modulation and evaluations of the contribution of the primary modulator to secondary scatter.

ACKNOWLEDGMENTS

The author would like to thank Michael Petrongolo and Tonghe Wang for their help with the acquisition of the experimental data used in this paper, and Dr. Anees H. Dhabaan in the Department of Radiation Oncology at Emory University for providing the Rando® phantom. Research reported in this publication was supported by the National Institute Of Biomedical Imaging And Bioengineering of the National Institutes of Health under Award No. R21EB019597 and R21EB021545. The content is solely the responsibility of the authors and does not necessarily represent the official views of the National Institutes of Health. The project was also partially supported by the Ministry of Science and Technology of China Key Research and Development Projects (Grant No. 2016YFC0101400) and by the National Natural Science Foundation of China (Grant No. 81671681).

CONFLICT OF INTEREST DISCLOSURE

The author has no COI to report.

[a]Electronic mail: leizhu@gatech.edu

[1]T. R. Fox, D. T. Nisius, H. Aradate, and Y. Saito, "Practical x-ray scatter measurements for volume CT detector design," Proc. SPIE **4320**, 808–814 (2001).
[2]M. Endo, S. Mori, T. Tsunoo, and H. Miyazaki, "Magnitude and effects of x-ray scatter in a 256-slice CT scanner," Med. Phys. **33**, 3359–3368 (2006).
[3]L. Zhu, Y. Xie, J. Wang, and L. Xing, "Scatter correction for cone-beam CT in radiation therapy," Med. Phys. **36**, 2258–2268 (2009).
[4]L. Zhu, J. Wang, and L. Xing, "Noise suppression in scatter correction for cone-beam CT," Med. Phys. **36**, 741–752 (2009).
[5]R. Fahrig, R. Dixon, T. Payne, R. L. Morin, A. Ganguly, and N. Strobel, "Dose and image quality for a cone-beam C-arm CT system," Med. Phys. **33**, 4541–4550 (2006).
[6]H. Gao, R. Fahrig, N. R. Bennett, M. Sun, J. Star-Lack, and L. Zhu, "Scatter correction method for x-ray CT using primary modulation: Phantom studies," Med. Phys. **37**, 934–946 (2010).
[7]H. Gao, L. Zhu, and R. Fahrig, "Modulator design for x-ray scatter correction using primary modulation: Material selection," Med. Phys. **37**, 4029–4037 (2010).
[8]H. Gao, L. Zhu, and R. Fahrig, "Optimization of system parameters for modulator design in x-ray scatter correction using primary modulation," Proc. SPIE **7622**, 76222A–76229A (2010).
[9]L. Zhu, N. R. Bennett, and R. Fahrig, "Scatter correction method for x-ray CT using primary modulation: Theory and preliminary results," IEEE Trans. Med. Imaging **25**, 1573–1587 (2006).
[10]L. Zhu, H. Gao, N. R. Bennett, L. Xing, and R. Fahrig, "Scatter correction for x-ray conebeam CT using one-dimensional primary modulation," Proc. SPIE **7258**, 725820 (2009).
[11]J. H. Siewerdsen and D. A. Jaffray, "Optimization of x-ray imaging geometry (with specific application to flat-panel cone-beam computed tomography)," Med. Phys. **27**, 1903–1914 (2000).
[12]J. H. Siewerdsen, D. J. Moseley, B. Bakhtiar, S. Richard, and D. A. Jaffray, "The influence of antiscatter grids on soft-tissue detectability in cone-beam computed tomography with flat-panel detectors," Med. Phys. **31**, 3506–3520 (2004).
[13]J. M. Boone, B. A. Arnold, and J. A. Seibert, "Characterization of the point spread function and modulation transfer function of scattered radiation using a digital imaging system," Med. Phys. **13**, 254–256 (1986).
[14]J. A. Seibert and J. M. Boone, "X-ray scatter removal by deconvolution," Med. Phys. **15**, 567–575 (1988).
[15]J. M. Boone and J. A. Seibert, "Monte Carlo simulation of the scattered radiation distribution in diagnostic radiology," Med. Phys. **15**, 713–720 (1988).
[16]Y. Kyriakou, T. Riedel, and W. A. Kalender, "Combining deterministic and Monte Carlo calculations for fast estimation of scatter intensities in CT," Phys. Med. Biol. **51**, 4567–4586 (2006).
[17]L. Shi, S. Vedantham, A. Karellas, and L. Zhu, "Library-based scatter correction for dedicated cone beam breast CT: A feasibility study," Proc. SPIE **9783**, 978330–978336 (2016).
[18]L. Shi, S. Vedantham, A. Karellas, and L. Zhu, "Library based x-ray scatter correction for dedicated cone beam breast CT," Med. Phys. **43**, 4529–4544 (2016).
[19]L. Zhu, N. Strobel, and R. Fahrig, "X-ray scatter correction for cone-beam CT using moving blocker array," Proc. SPIE **5745**, 251–258 (2005).
[20]T. Niu and L. Zhu, "Scatter correction for full-fan volumetric CT using a stationary beam blocker in a single full scan," Med. Phys. **38**, 6027–6038 (2011).
[21]T. Niu, M. Sun, J. Star-Lack, H. Gao, Q. Fan, and L. Zhu, "Shading correction for on-board cone-beam CT in radiation therapy using planning MDCT images," Med. Phys. **37**, 5395–5406 (2010).
[22]T. Niu, A. Al-Basheer, and L. Zhu, "Quantitative cone-beam CT imaging in radiation therapy using planning CT as a prior: First patient studies," Med. Phys. **39**, 1991–2000 (2012).
[23]Q. Fan, B. Lu, J. C. Park, T. Niu, J. G. Li, C. Liu, and L. Zhu, "Image-domain shading correction for cone-beam CT without prior patient information," J. Appl. Clin. Med. Phys. **16**, 65–75 (2015).

[24]P. Wu, X. Sun, H. Hu, T. Mao, W. Zhao, K. Sheng, A. A. Cheung, and T. Niu, "Iterative CT shading correction with no prior information," Phys. Med. Biol. **60**, 8437–8455 (2015).
[25]T. Niu and L. Zhu, "Overview of x-ray scatter in cone-beam computed tomography and its correction methods," Curr. Med. Imaging Rev. **6**, 82–89 (2010).
[26]R. Grimmer, R. Fahrig, W. Hinshaw, H. Gao, and M. Kachelriess, "Empirical cupping correction for CT scanners with primary modulation (ECCP)," Med. Phys. **39**, 825–831 (2012).
[27]K. Schorner, M. Goldammer, K. Stierstorfer, J. Stephan, and P. Boni, "Scatter correction method by temporal primary modulation in x-ray CT," IEEE Trans. Nucl. Sci. **59**, 3278–3285 (2012).
[28]L. Ritschl, R. Fahrig, M. Knaup, J. Maier, and M. Kachelriess, "Robust primary modulation-based scatter estimation for cone-beam CT," Med. Phys. **42**, 469–478 (2015).
[29]J. Star-Lack, J. Starman, P. Munro, A. Jeung, J. Richters, H. Mostafavi, and J. Pavkovich, "SU-FF-I-04: A fast variable-intensity ring suppression algorithm," Med. Phys. **33**, 1997 (2006).
[30]J. Sijbers and A. Postnov, "Reduction of ring artifacts in high resolution micro-CT reconstructions," Phys. Med. Biol. **49**, N247–N253 (2004).
[31]Y. Chen, Y. Song, J. Ma, and J. Zhao, "Optimization-based scatter estimation using primary modulation for computed tomography," Med. Phys. **43**, 4753–4767 (2016).
[32]J. Hsieh, E. Chao, J. Thibault, B. Grekowicz, A. Horst, S. McOlash, and T. J. Myers, "A novel reconstruction algorithm to extend the CT scan field-of-view," Med. Phys. **31**, 2385–2391 (2004).
[33]S. Schuller, S. Sawall, K. Stannigel, M. Hulsbusch, J. Ulrici, E. Hell, and M. Kachelriess, "Segmentation-free empirical beam hardening correction for CT," Med. Phys. **42**, 794–803 (2015).
[34]E. S. Ali and D. W. Rogers, "Quantifying the effect of off-focal radiation on the output of kilovoltage x-ray systems," Med. Phys. **35**, 4149–4160 (2008).
[35]X. Dong, T. Niu, X. Jia, and L. Zhu, "Relationship between x-ray illumination field size and flat field intensity and its impacts on x-ray imaging," Med. Phys. **39**, 5901–5909 (2012).